

# The temporal variability of soil moisture and surface hydrological quantities

Vivek K. Arora and George J. Boer

Canadian Centre for Climate Modelling and Analysis (CCCma), Meteorological Service of Canada, University of Victoria, Victoria, British Columbia, Canada.

Land surface models (LSMs) provide the connection between the atmosphere and the underlying land surface in general circulation models (GCMs) via fluxes of energy, moisture, and momentum. Soil moisture is a dominant characteristic affecting these fluxes and many researchers have investigated the role of soil moisture in influencing near-surface atmospheric variability and the effect of soil moisture anomalies on atmospheric circulation. Few studies have focused on the nature and causes of soil moisture variability itself.

Here we analyze the variability of land surface hydrological quantities in an AMIP 2 simulation made with the Canadian Centre for Climate Modelling and Analysis (CCCma) third-generation general circulation model (AGCM3). The land surface parameterization in this model is the comparatively sophisticated Canadian Land Surface Scheme (CLASS). Arora and Boer (2002) analyze, and compare with observations, the first order statistics of moisture budget quantities from the AMIP 2 simulation. Here, second order statistics namely variances and covariances, of surface hydrological quantities are assessed by comparison with observation-based estimates and related to soil moisture variance and the persistence time-scales of soil moisture anomalies.

Table 1: Comparison of globally averaged values of variances of AGCM3 precipitation (mm/day)<sup>2</sup>, evapotranspiration (mm/day)<sup>2</sup>, and soil moisture in the top 1 m layer (mm<sup>2</sup>) over land with observation-based and other estimates.

	AGCM3	Other estimate
Precipitation	1.65	1.59 (Xie and Arkin, 1996)
Evapotranspiration	0.19	0.15 (ECMWF reanalysis)
Soil Moisture	376	382 (VIC-2L hydro. model)

The variance of simulated monthly precipitation values is compared with the observation-based estimates of Xie and Arkin (1996) in Figure 1a. In the absence of an observation-based evapotranspiration data set, model evapotranspiration variance is compared with estimates obtained from ECMWF reanalysis (not shown). Globally averaged values over land are compared in Table 1. Model values of precipitation and evapotranspiration variance compare reasonably well with observation-based and reanalysis estimates, respectively. Figure 1b compares soil moisture variance estimates (for the top 1 m soil layer) with those simulated by the VIC-2L hydrological

model. Model estimates are qualitatively similar but generally somewhat larger than the VIC-2L estimates, although the globally averaged values compare well (Table 1).

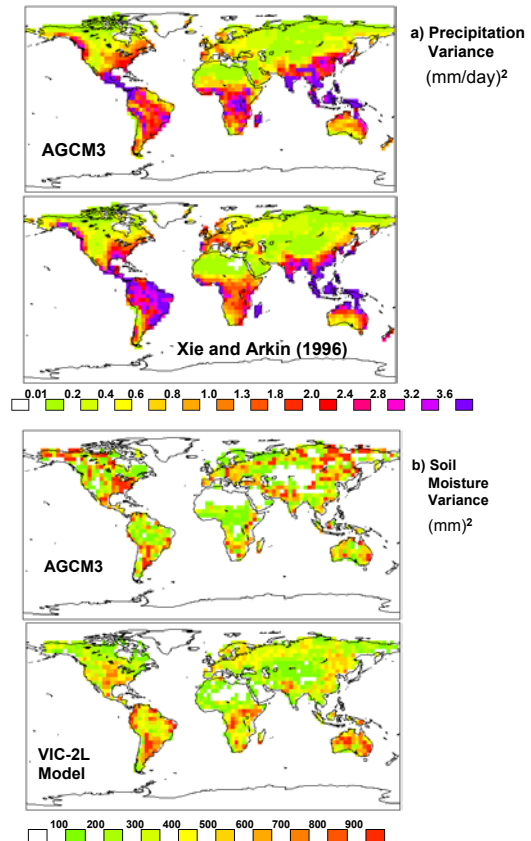


Figure 1: Comparison of AGCM3 precipitation variance with observed estimates of Xie and Arkin (1996) (a) and soil moisture variance with estimates from VIC-2L hydrological model (b).

We attempt to gain insight into the causes of soil moisture variability via a budget equation for the variances. The equation for soil moisture ( $W$ ) is,

$$\frac{dW}{dt} = G - E - R \quad (1)$$

where  $G$  is the moisture input into the soil (including precipitation, leaf drip, and snow melt),  $E$  is evapotranspiration, and  $R$  is runoff. Eqn. (1) can also be written in terms of deviations of the monthly hydrological quantities from their mean annual cycle as,

$$\frac{dW'}{dt} = \frac{W'_{t+n} - W'_t}{n} = G' - E' - R' = S' \quad (2)$$

where  $n=30$  days, and  $W'_{t+n}$  and  $W'_t$  are the daily soil moisture values at the end and beginning of each month. Squaring both sides of eqn. (2) and averaging yields,

$$\sigma_{daily}^2 = \frac{n^2}{[1-r(30)]} \left( \frac{\overline{G'^2} + \overline{E'^2} + \overline{R'^2} - 2\overline{G'R'}}{-2\overline{G'E'} + 2\overline{E'R'}} \right) = \frac{n^2}{[1-r(30)]} S'^2 \quad (3)$$

where  $\sigma_{daily}^2$  is the daily variance of soil moisture and  $r(30)$  is the lag 30-day soil moisture auto-correlation. Equation (3) can also be written in terms of monthly soil moisture variance ( $\sigma_w^2$ ) since

$$\sigma_w^2 = \sigma_{daily}^2 \frac{(1+C)}{n}; C = 2 \sum_{\alpha=1}^{n-1} \left( 1 - \frac{\alpha}{n} \right) r(\alpha) \quad (4)$$

where  $r(\alpha)$  is lag  $\alpha$ -day auto-correlation, as

$$\sigma_w^2 = \frac{n(1+C)}{2(1-r(30))} (S'^2). \quad (5)$$

Eqn. (5) illustrates how the variance and covariance terms of the moisture budget quantities ( $S'^2 = \overline{G'^2} + \overline{E'^2} + \overline{R'^2} - 2\overline{G'R'} - 2\overline{G'E'} + 2\overline{E'R'}$ ) and the “transfer function”  $[n(1+C)/2(1-r(30))]$  are connected to soil moisture variance  $\sigma_w^2$ . High values of soil moisture variance result when values of the transfer function and/or values of  $S'^2$  are high. The transfer function is essentially a measure of soil moisture persistence via the auto-correlation terms (eqn. 4) as seen by comparing it to the persistence estimated using monthly soil moisture anomaly time series in Figure 2. Soil moisture persistence is estimated as the average length of series of months with the same anomaly sign. Soil moisture persistence time-scales and the values of the transfer function are smaller in the tropics and larger at high-latitudes, consistent with the latitudinal dependence of soil moisture persistence on potential evaporation found in earlier studies.

AGCM3 estimates of monthly soil moisture variability are shown in Figure 3b and the variance and covariance term  $S'^2$  in Figure 3a. Model results indicate that soil moisture variability in the tropics is driven mainly by the variability of surface hydrological quantities, in particular precipitation (Figure 1) and runoff (not shown). In the tropics, although the persistence of soil moisture anomalies is short and values of the transfer function small (due to higher potential evaporation rates), higher values of soil moisture variance are still obtained because of high precipitation variability. At high-latitudes, however, higher soil moisture variability is linked to long persistence of soil moisture anomalies. Here, the variability of precipitation and other moisture budget quantities is low (Figure 3a); but since the persistence

time scales are longer and hence transfer function values are higher, the resulting soil moisture variance is high. As expected, soil moisture variance is low in regions with low precipitation such as the Sahara Desert, south-western U.S., and the Middle East.

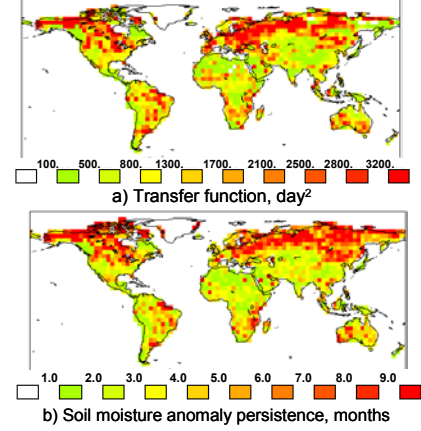


Figure 2: Transfer function (a) and persistence time scales of soil moisture anomalies (b).

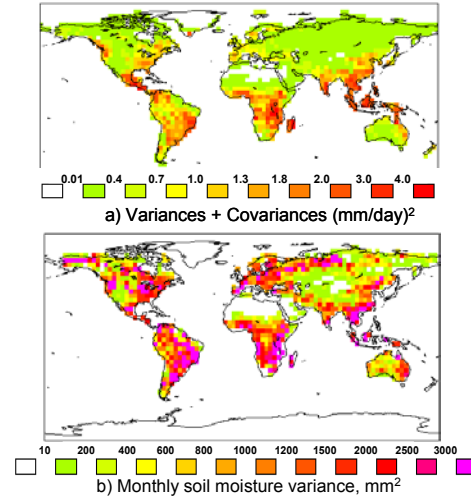


Figure 3: The sum of variances and covariances of moisture budget quantities (a) and AGCM3 simulated soil moisture variance (b).

## References

- Arora, V. K. and G. J. Boer, 2002, A GCM-based assessment of simulated global moisture budget and the role of land-surface moisture reservoirs in processing precipitation, *Clim. Dyn.*, 20(1), 13-29.
- Xie, P., and P.A. Arkin, 1997, Global precipitation: a 17-year monthly analysis based on gauge observations, satellite estimates, and numerical model outputs. *Bull. Ame. Meteorol. Soc.*, 11(78), 2539-2558.

Address any correspondence to Vivek.Arora@ec.gc.ca or George.Boer@ec.gc.ca.

## Impact of an IPCC-B2 scenario on Mediterranean sea temperature

Michel Déqué, Florence Sevault and Samuel Somot  
Météo-France/CNRM Toulouse France

A coupled climate simulation of the B2 IPCC scenario has been conducted with ARPEGE-Climate atmosphere model coupled with OPA ocean model (Douville et al., 2002). These two global models have a resolution of  $2.8^\circ$  and  $2^\circ$  respectively. This integration starts in 1950 with climatological conditions and undergoes during 150 years a radiative forcing with prescribed concentrations of carbon dioxide, methane, nitrous oxide, CFCs, and sulphate aerosols. These concentrations follow observations till 2000, then IPCC-B2 projections.

Decadal mean SST anomalies are extracted from this first simulation. A second simulation in uncoupled mode is performed with a high resolution version of ARPEGE-Climate (Gibelin and Déqué, 2003). This global model has a resolution of  $0.5^\circ$  in the Mediterranean sea, increasing to  $4.5^\circ$  at the antipodes. This 140-year simulation starts in 1960 and uses observed monthly SSTs till 2000, then artificial SSTs obtained by blending observed data with the decadal SST anomalies calculated from the coupled simulation (each calendar month having a different anomaly). The radiative forcing is exactly the same as in the coupled simulation. The radiative and SST constraints are consistent over the Mediterranean sea since the difference in the surface heat flux between 2070-2099 and 1960-1989 is almost zero, given the interannual variability. In other words, the raise in SST balances the increased downward radiation. This property, obvious in coupled mode, is obtained in forced mode since we use the same physical parameterizations and since the impact of horizontal resolution on the large-scale flux impact is negligible.

A third simulation has been produced with a regional version of the OPA ocean model. This version has  $0.125^\circ$  resolution and covers the whole Mediterranean sea (not the Black sea). A buffer zone in the near Atlantic with a strong relaxation towards climatology allows to simulate the Gibraltar straits flow. The river run-off (including the Black sea flow) is simulated by a surface salinity relaxation. The simulation lasts 130 years and is driven by the daily heat, water, and momentum fluxes from the high resolution atmosphere model from 1970 through 2099. The heat flux is recalculated as a function of SST by a linear correction. For the sake of simplicity rather than realism, we neglect the impact of the hydrological cycle in this simulation. In fact the hydrologic cycle decreases by  $0.3$  mm/day over the Mediterranean sea between the first 30 and the last 30 years of the atmosphere simulation. But we maintain the surface salinity relaxation constant, as well as the Atlantic buffer-zone. This experiment is more a sensitivity study to heat fluxes than an actual scenario. We will restrict our analysis to sea temperature at different level, and discard the salinity field.

Figure 1 shows the trend in annual mean temperature in three layers for three different sub-basins (western basin, Adriatic sea, eastern basin). The observed climatological conditions in the western basin are  $15.1$ ,  $13.5$  and  $12.9^\circ\text{C}$  in the 3 layers from top to bottom. In the Adriatic sea, the values are  $14.9$ ,  $13.6$  and  $13.2^\circ\text{C}$  respectively. In the eastern basin, the values are  $17.2$ ,  $14.5$  and  $13.4^\circ\text{C}$  respectively. The model starts in a slightly colder state than the clima-

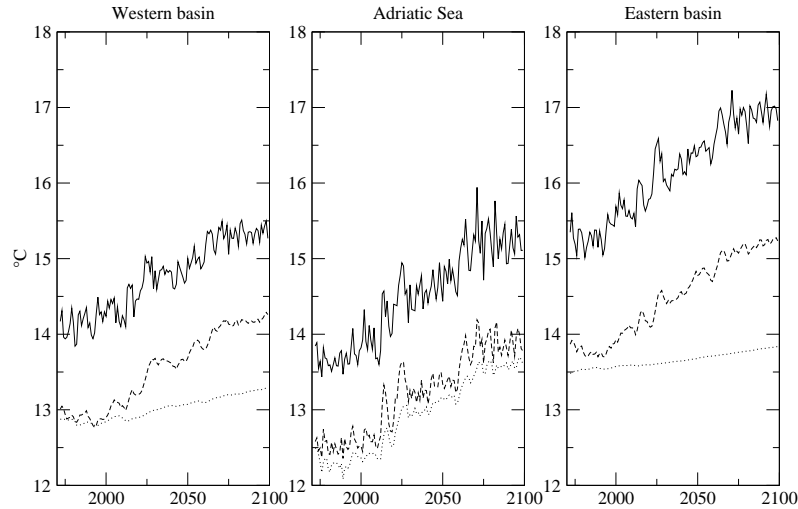


Figure 1: Annual mean sea temperature ( $^{\circ}\text{C}$ ) for the upper (0-150m; solid), middle (150-600m; dash), and lower (600m-bottom; dot) layers in the three basins of the Mediterranean sea, as simulated in the 130-year ocean model integration.

tological conditions. In the western basin, the upper layer warms up linearly by  $1.5^{\circ}\text{C}$  with some interannual variation. The middle layer warms up by the same amount, but the warming is delayed by a few decades. The lower layer warms up by only  $0.5^{\circ}\text{C}$  with some delay. A similar behavior is obtained in the eastern basin, except that the upper layer warming is more intense ( $2^{\circ}\text{C}$ ). The Adriatic sea is smaller and shallower than the other two basins. The warming in the 3 layers (the lower layer covers less than half of the basin) is similar and delayed in the middle and lower layer.

This experiment shows that the surface warming penetrates into the deep ocean in less than one century, despite the stabilization of the vertical profile. A next question to address is whether the expected increase in surface salinity will increase further the warming by modifying the thermohaline circulation. Further simulations in a more realistic way, including fully coupled simulations, will help our understanding of the impact of anthropogenic climate change on the Mediterranean sea.

## References

- Douville, H., Chauvin, F., Planton, S., Royer, J.F., Salas y Méliá, D., and Tyteca S., 2002: Sensitivity of the hydrological cycle to increasing amounts of greenhouse gases and aerosols. *Clim. Dyn.*, **20**, 45-68.
- Gibelin, A.L., and Déqué, M., 2003: Anthropogenic climate change over the Mediterranean region simulated by a global variable resolution model. *Clim. Dyn.*, **20**, 327-339.

## Joint Analysis of Climatic Changes of Surface Temperature and Cloudiness Vertical Structure in Antarctic Region on base CARDS

Irina V. Chernykh, Oleg A. Alduchov

*Russian Research Institute of Hydrometeorological Information- Word Data Center, Obninsk, Russia,*

*E-mails: [civ@meteo.ru](mailto:civ@meteo.ru) , [aoa@meteo.ru](mailto:aoa@meteo.ru)*

In previous study it was shown that climatic changes of cloudiness vertical structure are space inhomogeneous (Chernykh et al. 2001). Also increasing of cloud amount at the station South Pole was detected (Neff, 1999). In this paper joint analysis of climatic changes of surface temperature and cloudiness vertical structure in different atmospheric layers (0-2 km, 2-6 km, 6-10 km, 0-10 km) for nine coastal Antarctic stations (Table 1) is presented. For researches Aerological dataset CARDS (Eskridge et al. 1995) for period 1964-2001 years was used.

Chernykh and Eskridge method was used to determine cloud amount and boundaries from temperature and humidity profiles [Chernykh and Eskridge 1996]. Trends in anomalies for all parameters were calculated by linear regression with using the measuring data with provision for correlation dependence in time.

As it follows from previous researches (Comiso, 2000) and Table 2, values and sign of trends in surface temperature depend from station, period of observations and season.

In atmospheric layer 0-10 km for all studied stations, with exception Bellingshausen, number of cloud layers with cloud amount 0-100% of the sky increases (Table 3) and total thickness, on the contrary, decreases (Table 4). Only for Bellingshausen number of cloud layers decreases and total thickness increases. Note, that highest warming is detected namely for Bellingshausen (Table 2). Low boundary is stable or decreases. High boundary is stable or increases for all station, with exception Bellingshausen, for which it decreases (Table 5).

For atmospheric layers 0-2 km and 2-6 km number and total thickness of cloud layers trends have the same tendencies (Table 3, Table 4). It will be observed, that for most of stations, placed in Eastern Antarctica, the highest decreasing of total thickness take place for low clouds and highest increasing of cloud layers number – for middle and high clouds. Note, that for most stations, stability of cloud layers total thickness go with its number stability or increasing only for high clouds.

TABLE 1. List of stations

Station	Index	Latitude	Longitude	Height (m)	Period
Novolazarevskaya	89512	-70.75	11.8	130	1969.12-2001.12
Syowa	89532	-69.00	39.6	21	1969.10-2001.12
Mawson	89564	-67.60	62.9	16	1970.01-2001.12
Davis	89571	-68.58	78.0	13	1969.02-2001.12
Mirny	89592	-66.55	93.0	30	1969.10-2001.12
Casey	89611	-66.25	110.6	15	1967.02-2001.12
McMurdo	89664	-77.85	166.7	24	1964.01-2001.12
Bellingshausen	89050	-62.18	-58.9	42	1970.02-1999.01
Halley Bay	89022	-75.50	-26.6	29	1966.12-2001.12

TABLE 2. Surface temperature anomalies trends °C decade<sup>-1</sup>, calculated by linear regression on base CARDS by using measured values with provision for correlation dependence in time. The trend values at the 95% significant level marked by \*; other trends are at significant level not less than 50%. Seasons: I - December - February; II – March- May; III – June- August; IV – September-November.

Station	Seasons/ Year				
	I	II	III	IV	Year
Novolazarevskaya	-	-0.78*	0.22	-0.26	-0.20
Syowa	-0.17	-0.80*	-	-0.25	-0.29*
Mawson	-0.46*	-0.40	-	-0.21	-0.25*
Davis	-0.12	-	-	0.51	-
Mirny	-0.30	-0.53	-	-	-0.16
Casey	-0.20	-0.90*	0.35*	-	-0.21
McMurdo	0.16	-0.2	0.23*	0.45	0.20*
Bellingshausen	0.33*	0.65*	0.81	-	0.40*
Halley Bay	-	-0.45	0.30	-0.20	-0.12

TABLE 3. Means (m, meters) and decadal changes (tr, number decade<sup>-1</sup>) for number of cloud layers with cloud amount 0-100% of the sky for different atmospheric layers. The trend values at the 95% significant level marked by \*; other trends are at significant level not less than 50%.

Station	Atmospheric layer							
	0-2 км		2-6 км		6-10 км		0-10 км	
	m	tr	m	tr	m	tr	m	tr
Novolazarevskaya	1.8	0.05*	2.4	0.23*	2.6	0.26*	6.2	0.44*
Syowa	1.9	0.15*	2.7	0.17*	2.2	-	5.0	-
Mawson	2.1	0.33*	2.9	0.67*	2.8	0.77*	7.4	1.99*
Davis	2.1	0.36*	2.8	0.83*	2.7	0.86*	7.3	2.40*
Mirny	1.8	0.05*	2.2	0.21*	2.6	0.35*	6.0	0.63*
Casey	2.1	0.31*	2.9	0.70*	2.9	0.75*	7.5	1.90*
McMurdo	2.2	0.11*	3.1	0.11*	3.1	-	8.0	-
Bellingshausen	1.9	-0.02	2.1	0.03	2.4	-	5.8	-0.17*
Halley Bay	1.9	0.09*	2.4	0.42*	2.6	0.50*	6.4	1.22*

TABLE 4. Means (m, meters) and decadal changes (tr, meters decade<sup>-1</sup>) for total thickness of cloud layers with cloud amount 0-100% of the sky for different atmospheric layers. The trend values at the 95% significant level marked by \*; other trends are at significant level not less than 50%.

Station	Atmospheric layer							
	0-2 км		2-6 км		6-10 км		0-10 км	
	m	tr	m	tr	m	tr	m	tr
Novolazarevskaya	600	-23	1070	-42*	1414	-41*	3000	-57*
Syowa	560	-17*	1076	-	1507	-	2493	-
Mawson	634	-41*	1083	-27*	1367	-	3078	-92*
Davis	620	-72*	1096	-23*	1332	-	3089	-151*
Mirny	547	-62*	1017	-68*	1368	-75*	2832	-159*
Casey	602	-69*	1092	-24*	1322	64*	2999	-
McMurdo	604	-21*	1074	21	1366	-	2962	-
Bellingshausen	587	14	968	-	1356	-	2781	60*
Halley Bay	508	-35*	1023	-36*	1304	-128*	2740	-154*

TABLE 5. Means (m, meters) and decadal changes (tr, meters decade<sup>-1</sup>) for low and high boundaries of cloud layers with cloud amount 0-100% of the sky for atmospheric layer 0-10 км. The trend values at the 95% significant level marked by \*; other trends are at significant level not less than 50%.

Station	Low boundary		High boundary	
	m	tr	m	tr
Novolazarevskaya	852	-41*	9435	12
Syowa	770	-	7325	-
Mawson	652	-28	9343	104*
Davis	590	-	9340	132*
Mirny	864	-30	9456	36*
Casey	576	-61*	9347	114*
McMurdo	545	-	9229	-
Bellingshausen	723	-66*	9402	-14
Halley Bay	1029	-184*	9319	67

This study is useful to gain insight into climate change in Antarctica. Further researches should be useful. The research was partly supported by RBRF, project 01-05-65285.

## References

- Eskridge, R. E., O. A. Alduchov, I. V. Chernykh, P. Zhai, S. R. Doty, and A. C. Polansky, 1995: A Comprehensive Aerological Reference Data Set (CARDS): Rough and systematic errors. *Bull. Amer. Meteor. Soc.*, **76**, 1959-1775.
- Chernykh I.V., O.A. Alduchov, and R. E. Eskridge, 2001: Trends in low and high cloud boundaries and errors in height determination of cloud boundaries. *Bull. Amer. Meteor. Soc.*, **82**, 1941-1947.
- Chernykh I. V. and R. E. Eskridge, 1996: Determination of cloud amount and level from radiosonde soundings. *J. Appl. Meteorol*, **35**, 1362-1369.
- Comiso J.C. , 2000: Variability and trends in Antarctic surface temperatures from in situ and satellite infrared measurements. *J. Climate*, **15**, No 10, 1674-1696.
- Neff, W.D. 1999: Decadal time scale trends and variability in the tropospheric circulation over South The Pole. *J. Geophys. Res.*, **104**(D22), 27217-27251

## **A 12-year (1987-1998) ensemble simulation of the U.S. climate with a variable-resolution stretched-grid GCM**

Michael S. Fox-Rabinovitz, ESSIC (Earth Sciences Interdisciplinary Center), University of Maryland, College Park, MD 20742-2465; and Data Assimilation Office, NASA/Goddard Space Flight Center, Greenbelt, MD 20771

Lawrence L. Takacs and Ravi C. Govindaraju, SAIC/General Sciences Corporation, Beltsville, MD 20705-2675; and Data Assimilation Office, NASA/Goddard Space Flight Center, Greenbelt, MD 20771

The GEOS (Goddard Earth Observing System) stretched-grid (SG) GCM and the GEOS SG-DAS (Data Assimilation System) have been developed and thoroughly tested over the last few years (Fox-Rabinovitz et al. 1997, 2000, 2001, 2003, Fox-Rabinovitz 2000). The model and system are used for regional climate experiments for seasonal, annual, and multiyear time scales.

The variable-resolution GEOS SG-GCM has been used for long-term/multiyear limited ensemble integrations with a relatively coarse, 60 to 100 km, regional resolution over the U.S. The experiments have been run for the 12-year period, 1987-1998, which includes the recent ENSO cycles. Initial conditions 1-2 days apart are used for ensemble members. The goal of the experiments is analyzing the long-term SG-GCM ensemble integrations in terms of their potential in reducing the uncertainties of regional climate simulation while producing realistic mesoscales.

The ensemble integration results are analyzed for both prognostic and diagnostic fields. A special attention is devoted to analyzing the variability of precipitation over the U.S. The internal variability of the SG-GCM has been assessed. The ensemble means appear to be closer to the verifying analyses than

the individual ensemble members. The ensemble means capture realistic mesoscale patterns, especially those of induced by orography. Two ENSO cycles have been analyzed in terms of their impact on the U.S. climate, especially on precipitation. The ability of the SG-GCM simulations to produce long-term regional climate anomalies has been confirmed. However, the optimal size of the ensembles depending on fine regional resolution used is still to be determined.

It is noteworthy that the SG-GCM ensemble simulations are performed as a preparation for the international SGMIP (Stretched-Grid Model Intercomparison Project) that is under way with participation of the major centers and groups from the U.S., Canada, France, and Australia employing the SG-approach for regional climate modeling. The SGMIP results are planned to be submitted later to AMIP-II as a regional project.

### References

Fox-Rabinovitz, M. S., L.V. Stenchikov, M. J. Suarez, L. L. Takacs, 1997: A finite-difference GCM dynamical core with a variable resolution stretched-grid, *Mon. Wea. Rev.*, Vol. 125, No. 11, 943-2968.

Fox-Rabinovitz, M. S., L.V. Stenchikov, M. J. Suarez, L. L. Takacs, and R.C. Govindaraju, 2000: An uniform and variable resolution stretched-grid GCM dynamical core with real orography, *Mon. Wea. Rev.*, Vol. 128, No. 6, 1883-1898.

Fox-Rabinovitz, M. S., 2000: Regional climate simulation of anomalous U.S. summer events with a variable-resolution stretched-grid GCM, *J. Geophys. Res.*, v. 105, No. D24, pp. 29,635-29,646.

Fox-Rabinovitz, M.S., L.L. Takacs, and M.J. Suarez, 2001: A Variable Resolution Stretched Grid GCM: Regional Climate Simulation. *Mon. Wea. Rev.*, Vol. 129, No. 3, pp. 453-469.

Fox-Rabinovitz, M.S., L.L. Takacs, and R.C. Govindaraju, 2003: A stretched-grid GCM and DAS with multiple areas of interest: Studying the anomalous regional climate events of 1998. *J. Geophys. Res.*, in press.

# Teleconnections and upscaling relationships for the Eemian

Nikolaus Groll (groll@gkss.de), Martin Widmann and Julie M. Jones

Institute of Coastal Research, GKSS Research Centre, Geesthacht, Germany

The aim of our model based study is to investigate the hemispheric circulation differences between Eemian (last interglacial) and Holocene in terms of teleconnections (Wallace and Gutzler 1981) and to find a statistical upscaling model, which links local proxy data to the intensities of large scale circulation patterns, for further reconstruction from proxy data. As a coupled atmosphere-ocean GCM we use a 1000 year long control run (CTRL) from the ECHO-G with Milankovitch-forcing for the Eemian (125kyBP) (MPI-Met Hamburg, F. Kaspar, pers.com.). We compare the Eemian CTRL with a CTRL with preindustrial greenhouse -gas concentration (270ppm CO<sub>2</sub>) (MPI-Met Hamburg, S. Lorenz, pers.com.).

Teleconnections (here, strongest negative correlation between one gridpoint and any other) (Fig.1) are slightly different in the two periods. In Fig.2 the difference (Holocene minus Eemian) between the teleconnection is shown. In particular the Pacific region (corresponding to PNA) shows different correlations, but also over the North Atlantic (NAO) we see stronger correlations in summer for the Eemian. Further studies for explanations and possible impacts from these results are planned.

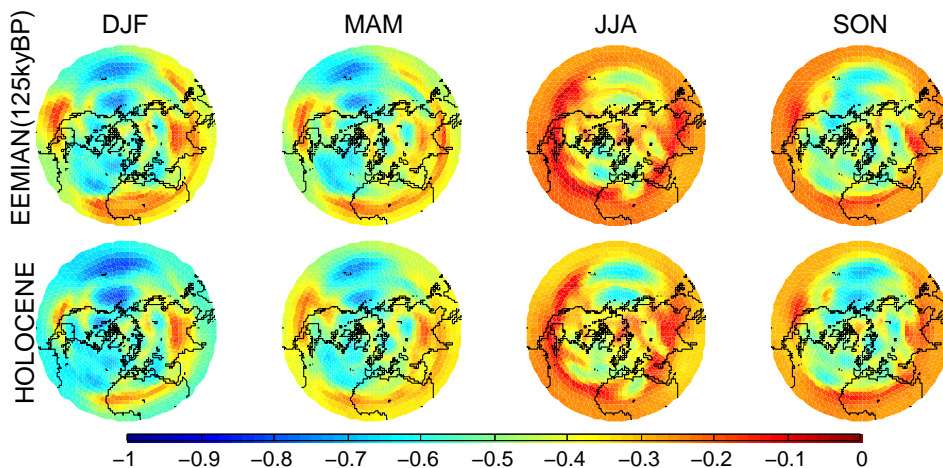


Figure 1: Teleconnections for 500hPa geopotential height

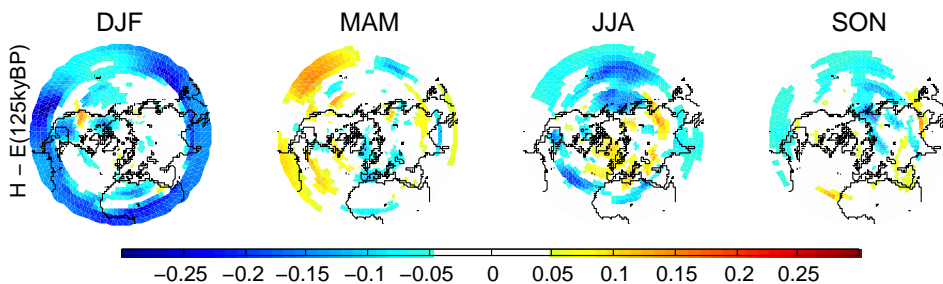


Figure 2: Differences of teleconnections for 500hPa geopotential height (Holocene - Eemian 125ky BP), only differences  $> 0.05$  are shown,  $> 0$  ( $< 0$ ) stronger (weaker) negative Eemian correlation.

Upscaling has been successfully applied for the Late Holocene, for instance to reconstruct large-scale temperature (Mann et al. 1998, Briffa et al. 2001, Esper et al. 2002), or circulation anomalies (Cook et al. 2001, Jones and Widmann 2003) from proxy data. Since the Eemian

climate may have substantially differed from current conditions, we cannot fit the upscaling model within the instrumental period, therefore we use simulated GCM climate as a surrogate to derive the relationship between regional climate and large-scale circulation. These relationships can then be applied to local climate information derived from proxy data by local transfer functions. Reconstructed temperature series from Germany and France for the period around 125 ky BP are available. The sites are located in highly correlated, adjacent grid cells of the GCM ECHO-G, and therefore all reconstructions represent the central European temperature on the scales resolved by the model. Thus the relation between simulated central European temperature and the SLP field has been investigated by means of regression maps (Fig.3). In summer higher central European temperatures are associated with high pressure over central Europe. In the other seasons a strong link between European temperatures and larger-scale pressure anomalies, similar but not identical to the (N)AO, associated with southwesterly (northeasterly) advection of warm (cold) air masses becomes evident. Significant differences between the Eemian and the Holocene are simulated in spring, while in the other seasons the upscaling relationships in the two periods are very similar.

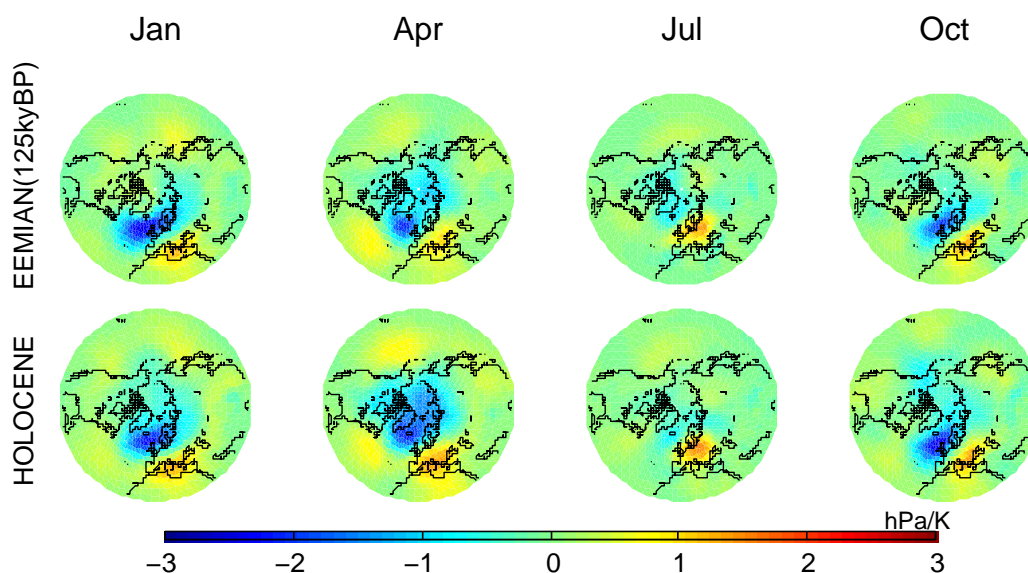


Figure 3: Regression coefficients of SLP against central European temperature from equilibrium run with the ECHO-G model for Eemian and Holocene

## References

- Briffa, K.R., T.J. Osborn, F.H. Schweingruber, I.C. Harris, P.D. Jones, S.G. Shiyatov and E.A. Vaganov, 2001: Low frequency temperature variations from a northern tree-ring density network. *J. Geophys. Res.*, **106**, 2929-2941.
- Cook, E.R., R.D. D'Arrigo and M.E. Mann, 2002: A very-well verified, multiproxy reconstruction of the winter North Atlantic Oscillation Index since A.D.1400 *J. Clim.*, **15**, 1754-1764.
- Esper, J., E.R. Cook and F.H. Schweingruber, 2002: Low-frequency signals in long tree-ring chronologies for reconstructing past temperature variability. *Science*, **295**, 2250-2254.
- Jones, J.M. and M. Widmann, 2003: Instrument- and tree-ring-based estimates for the Antarctic Oscillation. *J. Clim.*, accepted.
- Mann, M.E., R.S. Bradley and M.K. Hughes, 1998 Global-scale temperature patterns and climate forcing over the past six centuries. *Nature*, **392**, 779-787.
- Wallace, J.M. and D.S. Gutzler, 1981: Teleconnection in the Geopotential Height Fields during the Northern Hemisphere Winter.. *Mon. Wea. Rev.*, **109**, 784-812.

# Chemistry and Climate Studies with the Met Office Unified Model

R.S. Harwood, R.M. Doherty, I.A. MacKenzie, and D.S. Stevenson  
School of GeoSciences, University of Edinburgh,  
King's Buildings, Edinburgh, EH9 3JZ, UK. (iam@met.ed.ac.uk)

## Introduction

A number of studies of the impact of natural and anthropogenic emissions and interannual variability on atmospheric composition and climate are being performed with the Met Office Unified General Circulation Model (UM).

## Modelling the atmospheric impact of the 1783-1784 Laki eruption

A chemistry-transport model (STOCHEM) coupled to the UM has been used to simulate the atmospheric impact of the 1783-1784 Laki volcanic eruption from Iceland [Stevenson *et al.*, 2003]. This effusive eruption added about 60 Tg(S) to the troposphere and lower stratosphere over an 8 month period, starting in June. By comparison, present-day anthropogenic emissions total about 70 Tg(S)/yr, and the 1991 explosive eruption of Mt. Pinatubo added about 20 Tg(S) to the mid-stratosphere. Figure 1 shows zonal, JJA mean sulphate concentrations simulated by the model, for the present-day, the pre-industrial, and for two Laki simulations with differing height profiles of emissions (Lo: evenly distributed 0-9 km; Hi: 25% (0-3 km), 75% (9-13 km)). The sulphate has a mean atmospheric lifetime of 6-9 days, although the local lifetime is of order a few months in the lower stratosphere. When added to a climate model, the aerosol generates a Northern Hemisphere mean top of the atmosphere radiative forcing of up to  $-6 \text{ Wm}^{-2}$  for a few months, before decaying fairly rapidly as the eruption ceases [Highwood and Stevenson, 2003]. The Hi scenario produces a climate cooling in the Northern Hemisphere of order  $-0.2 \text{ K}$  for the year 1783, in good agreement with the limited data for the time. This modelling study has many areas of uncertainty, but represents the first attempt to apply detailed atmospheric models to the climate impact of large-scale effusive volcanic eruptions.

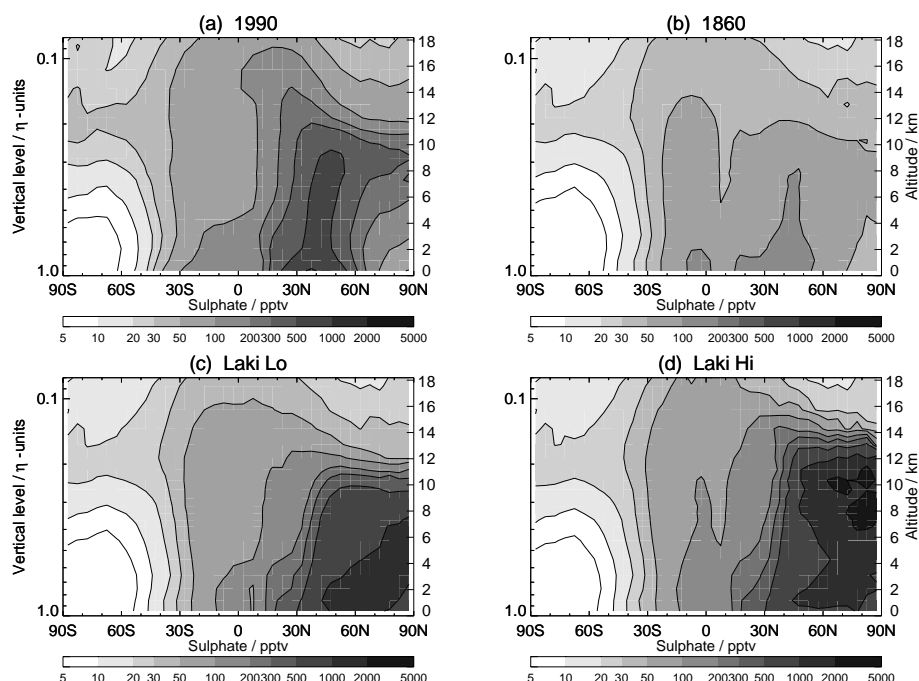


Figure 1: Sulphate concentrations from different model simulations—see text for details.

## The influence of ENSO on tropospheric ozone variability

Results from a modelling experiment using the HadCM3 UM coupled to the STOCHEM chemistry model are being examined to investigate the role of interannual variability in climate on tropospheric ozone. The IPCC SRES A2 future high growth emissions scenario is used to provide the climate forcing for 1990-2100 and also the (annual smoothly growing) anthropogenic emissions input to the chemistry model. Natural emissions are annually invariant, hence the modelled ozone variability arises solely from interactions between climate and chemistry.

ENSO is the dominant mode of variability in the tropics on interannual timescales. Correlation maps using the Niño3 index show the patterns of surface temperature and precipitation associated with ENSO for the last 30 years of

the experiment (Figure 2). Tropospheric column ozone analysed from this experiment, also shown, exhibits ENSO-like spatial patterns, with positive coefficients suggesting enhanced ozone over Indonesia, and negative coefficients suggesting suppressed ozone over the central and western Pacific, under El Niño like conditions. Over Indonesia, lower temperatures and humidities during El Niño give rise to lower OH and ozone destruction rates and higher net chemical production of ozone. In addition to reduced humidities, dynamical changes in convection during El Niño may also be contributing to the simulated ozone pattern. The converse situation occurs over the central and western equatorial Pacific. Variations in biomass burning and lightning emissions are not included, but are likely to be major contributors in the real atmosphere.

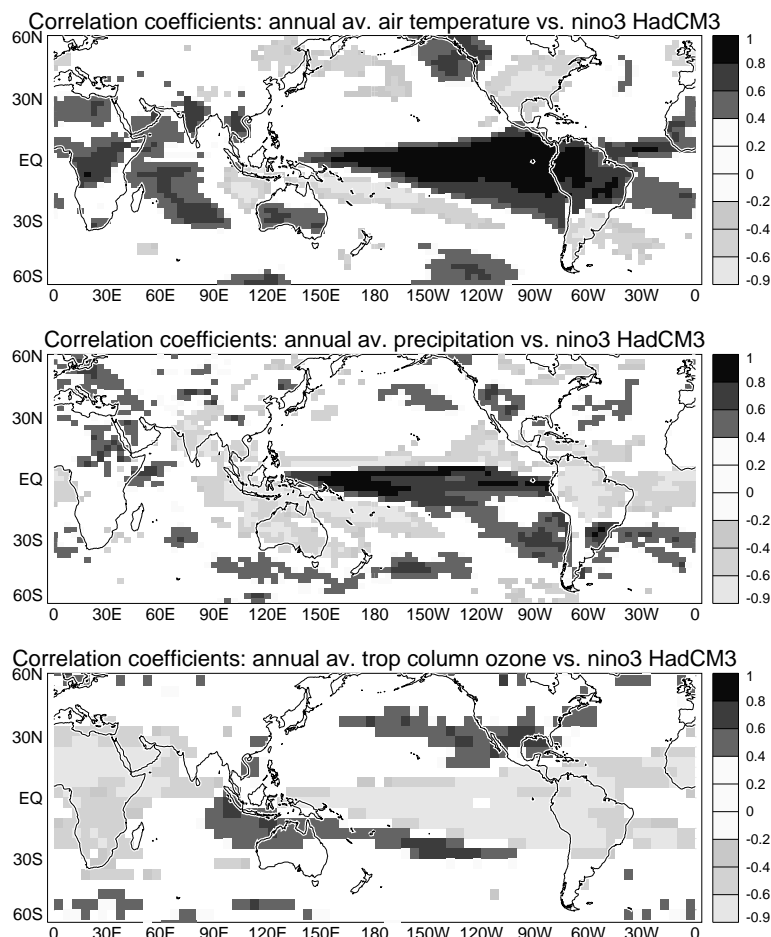


Figure 2: Correlation coefficients between the Niño3 ENSO index and surface temperature, precipitation and tropospheric ozone column for 30 years of a UM simulation (only values significant above the 95% level are plotted).

### Impact of methane-derived water vapour on future middle-atmospheric climate

A recently-completed study with the UM suggests that under the IPCC SRES B2 emission scenario, the H<sub>2</sub>O increase stemming from stratospheric oxidation of increased atmospheric CH<sub>4</sub> contributes approximately 10% of the total middle-atmospheric cooling occurring between 1995 and 2060 [Mackenzie and Harwood, 2003]. The ~25% fraction of the increase in polar stratospheric clouds in 2060 compared with 1995 which is attributable to the extra H<sub>2</sub>O (the remainder being due to the reduced temperatures) makes the 2060 Arctic ozone loss ~15% greater than it would otherwise be. (Albeit, the loss is still much less than in 1995 owing to the reduced chlorine loading.)

### References

- Highwood, E. J. and D. S. Stevenson, Atmospheric Impact of the 1783-84 Laki eruption: Part II Climatic effect of sulphate aerosol, in press, Atmos. Chem. Phys. Disc.
- MacKenzie, I. A. and R. S. Harwood, Middle-atmospheric response to a future increase in humidity caused by increased methane emission, submitted to J. Geophys. Res., 2003.
- Stevenson, D. S., C. E. Johnson, E. J. Highwood, V. Gauci, W. J. Collins and R. G. Derwent, Atmospheric Impact of the 1783-84 Laki eruption: Part I Chemistry modelling, Atmos. Chem. Phys. Disc. 3, 551-596, 2003. (<http://www.copernicus.org/EGU/acp/acpd/3/551>).

# REGIONAL CLIMATE SIMULATIONS OF THE 1990 NORTH AMERICAN SUMMER MONSOON

Hann-Ming Henry Juang, Yucheng Song, and Kingtse Mo

Environmental Modeling Center  
NOAA/NWS/National Centers for Environmental Prediction,  
5200 Auth Rd., Camp Springs, MD 20746, USA ; Henry.Juang@noaa.gov

The NCEP Regional Spectral Model (RSM) is used to simulate the North American summer monsoon for the year 1990. This year was proposed by the NAME (North American Monsoon Experiment) for regional climate modeling. Two domains are proposed for all regional models to integrate during the summer monsoon. The big domain covers the area of 15-40 N and 125-70 W, and the RSM is configured with 40 km grid spacing over this domain. The small domain covers the area of 18-37N and 117-101W, and the RSM is configured with 20 km grid spacing over the smaller domain.

The big domain is tested with a multi-month integration from May to October. The result from the continuous run over this period showed a bias toward drying out the soil moisture with less rainfall after August. The run from day one of each month provides a better result when compared to observations. The bias in the continuous multi-month integration may be due to the soil moisture problem in the land model. However, the single month runs show nearly no monsoon rainfall over the Arizona and New Mexico (AZNM) areas, which are in the geographic area of the summer monsoon.

In order to investigate the ill-simulated monsoon over AZNM, the small domain, higher resolution integration is performed using better surface conditions including terrain. The high-resolution terrain provided better resolution of the surface temperature gradient, which resolves the low level jet along the Gulf of California, that carries moisture from south to north. The low-level moisture jet provides low level atmospheric instability over the AZNM to produce ample rainfall. Thus, the high resolution of the model to resolve the low-level jet along the Gulf of California is essential. Though the time sequence of the rainfall events are well simulated, the intensity of the significant event still is not simulated well.

The problem of the horizontal diffusion over the model sigma coordinate is identified as a possible error causing less rainfall in the significant event. The modification of the horizontal diffusion on the pressure surface instead of the model sigma coordinate was developed and tested successfully (see Fig. 1), thus the rainfall intensity of the significant event is better simulated (see Fig. 2). A simple diagnostic study shows that the moisture is better distributed in the case of horizontal diffusion on the pressure surface than is the case on the sigma surface. Thus the low-level jet carried more moisture northward, causing a better rainfall distribution and intensity, especially over AZNM areas.

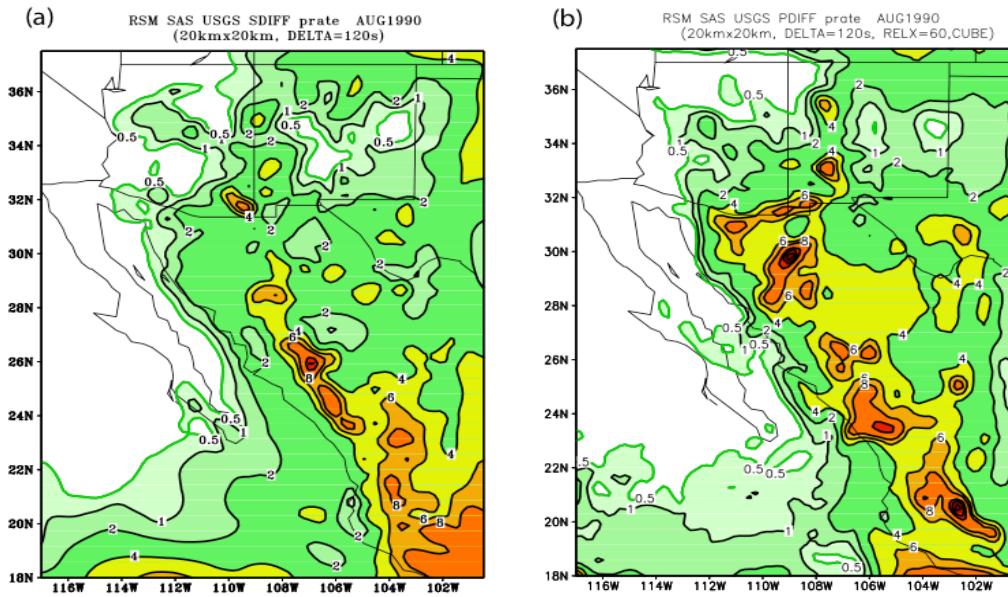


Fig. 1 Monthly accumulated rainfall for (a) perturbation diffusion on sigma surface and (b) full field diffusion on pressure surface for August 1990 from RSM with 20 km resolution.

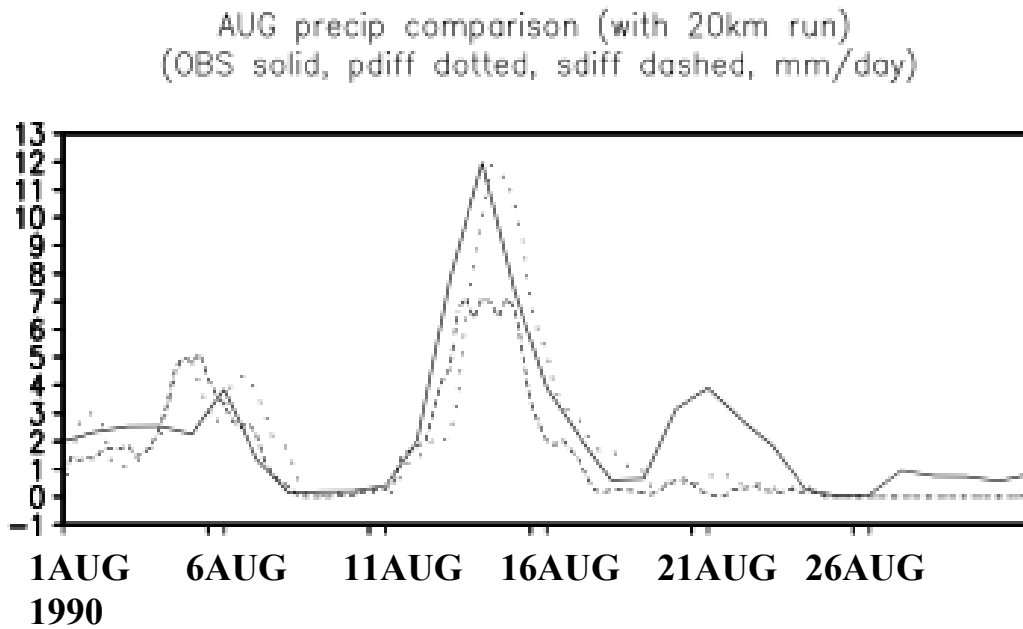


Fig. 2 Daily rainfall for August 1990 from observations (solid curve), results of diffusion on sigma surface (dashed curve) and results of diffusion on pressure surface (dotted curve).

## Model projections of extreme runoff (floods) in Siberian rivers basins

I. I. Mokhov and A.A Karpenko  
A.M.Obukhov Institute of Atmospheric Physics RAS  
3 Pyzhevsky, 119017 Moscow, Russia  
mokhov@omega.ifaran.ru

Significant variations of hydrological regime have been noted during the XX century in different regions. Strong floods during last years are associated with largest Siberian rivers, including Lena, Yenisei and Ob rivers. These rivers have extended basins from the middle to the polar latitudes in the Siberian regions with a large warming during last decades. It is necessary to estimate future changes of extreme runoff and floods probability in the Ob, Yenisei and Lena rivers basins due to possible climate changes in the XXI century.

Water cycle changes in the Siberian rivers basins, including rivers runoff, from transient runs of coupled general circulation model ECHAM4/OPYC3 (Oberhuber 1993; Roeckner et al. 1996) and IAP RAS climate model (CM) of intermediate complexity (Petoukhov et al. 1998; Handorf et al. 1999; Mokhov et al. 2002) for the period 1860-2100 are analyzed (Mokhov and Khon 2002). Changes of greenhouse gases in the atmosphere in these numerical experiments were taken from observations for the 1860-1990 period and according to the IS92a scenario (Houghton et al. 1992) for the 1991-2100 period. For IAP RAS CM simulations with change only CO<sub>2</sub> content in the atmosphere are analyzed. The annual-mean river runoff was characterized by a difference between annual-mean precipitation and evaporation on river watersheds. Model simulations were compared with observations for the Ob (1930-1994), Yenisei (1936-1995) and Lena (1935-1994) rivers runoff (e.g., Duemenil et al. 2000).

Figure 1 shows cumulative distributions of normalized runoff (normalized to the maximum value in the XX century) of the Lena (a), Yenisei (b) and Ob (c) rivers from ECHAM4/OPYC3 simulations for XX (thin curve) and XXI (thin dashed curve) centuries as a whole in comparison with observations (bold curve). The bold dashed curves display the appropriate cumulative distributions from simulations for the period with available observations in the XX century. These cumulative distributions were compared with similar distributions from the IAP RAS CM simulations.

According to the ECHAM4/OPYC3 simulations the maximum Lena and Yenisei rivers runoff in the XXI century as a whole can be larger on 30% and 19% respectively in comparison to the XX century. The probability of exceeding in the XXI century of the XX century maximum runoff was found from the ECHAM4/OPYC3 simulations to be about 7% and 11% for the Lena and Yenisei rivers, respectively. No significant changes of the extreme Ob river runoff between XX and XXI centuries (as a whole) have been noted from the ECHAM4/OPYC3 simulations.

According to the IAP RAS CM simulations the maximum Lena, Yenisei and Ob rivers runoff in the XXI century as a whole can be larger on 60%, 13% and 37% respectively in comparison to the XX century. The probability of exceeding in the XXI century of the XX century maximum runoff was found from the IAP RAS CM simulations to be about 38%, 5% and 15% for the Lena, Yenisei and Ob rivers, respectively.

This work has been partly supported by the Russian Foundation for Basic Research.

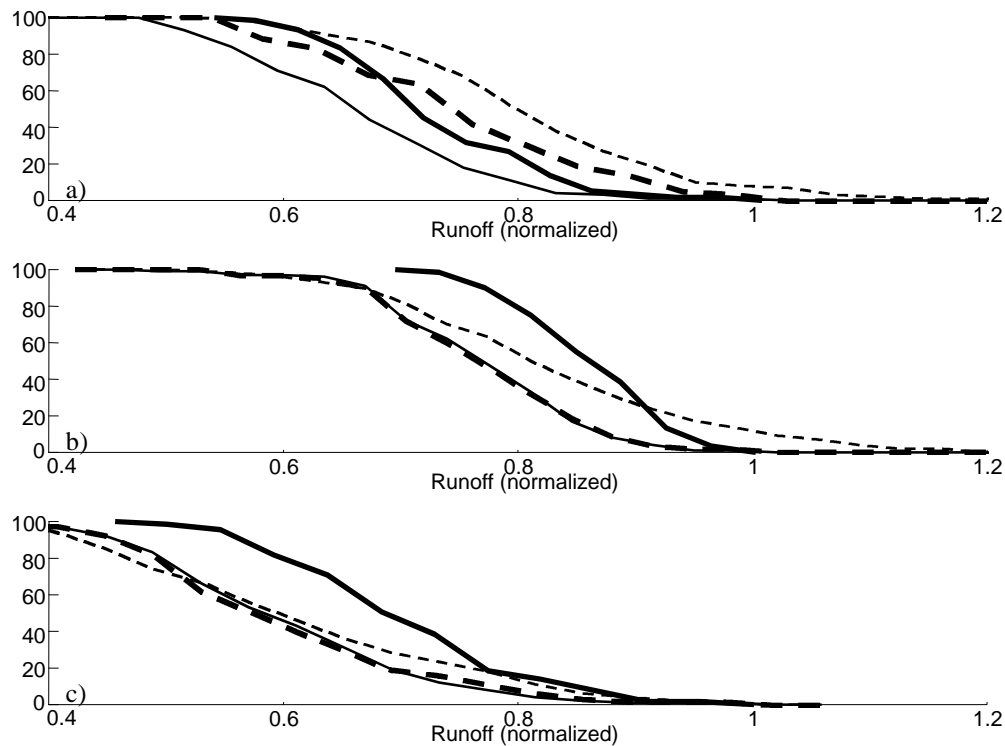


Fig.1.

## References

- Duemenil Gates, L., S. Hagemann, and C. Golz Observed historical discharge data from major rivers for climate model validation. Max-Planck-Institut fuer Meteorologie, Rep. No.307, 93pp.
- Handorf, D., V.K. Petoukhov, K. Dethloff, A.V. Eliseev, A. Weisheimer, and I.I. Mokhov, 1999: Decadal climate variability in a coupled atmosphere-ocean climate model of moderate complexity. *J. Geophys. Res.*, **104**, 27253-27275.
- Houghton, J.T., B.A. Callander, and S.K. Varney (eds), 1992: *Climate Change: The Supplementary Report to the IPCC Scientific Assessment*. Intergovernmental Panel on Climate Change. Cambridge University Press, 198 pp.
- Mokhov, I.I. and V.Ch. Khon, 2002: Hydrological regime in Siberian rivers basins: Model estimates of changes in XXI century. *Rus. Meteor. Hydrol.*, **8**, 77-93.
- Mokhov, I.I., P.F. Demchenko, A.V. Eliseev, V.Ch. Khon and, D.V. Khvorostyanov, 2002: Estimations of global and regional climate changes during XIX-XXI centuries on the basis of the IAP RAS model with anthropogenic forcing. *Izvestiya. Atmos. Oceanic Phys.*, **38**, 629-642..
- Oberhuber J.M., 1993: *The OPYC Ocean General Circulation Model*. Max-Planck-Institute for Meteorology. Rep. No.7. Hamburg, 130 pp.
- Petoukhov V.K., I.I. Mokhov, A.V. Eliseev, V.A. Semenov, 1998: *The IAP RAS global climate model*. Moscow, Dialogue-MSU. 110 pp.
- Roeckner E., K. Arpe, L. Bengtsson, M. Christoph, M. Claussen, L. Duemenil, M. Esch, M. Giorgetta, U. Schlese, U. Schulzweida, 1996: *The atmospheric general circulation model ECHAM4: Model description and simulation of present-day climate*. Max-Planck-Institute for Meteorology Rep. No.218. Hamburg. 90 pp.

# **Sensitivity of the vertical coupling of Northern wintertime annular modes to anomalous high-latitude surface heating**

*David Noone (dcn@caltech.edu)*

*Division of Geological and Planetary Science, California Institute of Technology  
1200 E. California Blvd, Pasadena, CA 91125, USA*

Throughout the atmospheric column, the first mode of variability in anomalies of wintertime geopotential height (and other parameters) is associated with an annular variation. These modes describe, in the positive phase, an intensification of the polar vortex, increased mid-latitude westerly winds, poleward migration of the baroclinic storm tracks and decreased polar temperatures. While it is generally considered that these are equivalent barotropic features, it is unclear how variations in the stratosphere and troposphere interact. This interaction is explored using results from the NCAR Community Climate Model (version 3.6.6) configured to a resolution of T31L26 using the “standard” boundary data (control simulation). To quantify the vertical coupling of the annular variations in the Northern Hemisphere, principal component (PC) analysis is performed on pressure surfaces independently throughout the atmospheric column for 10 years of twice daily wintertime (DJF) geopotential height anomalies. For each year, the temporal series of the first mode (PC1) at some level of interest (say, 500 hPa) is correlated with PC1 found at all other levels. The resulting correlation mapping is presented in Figure 1 as a function of temporal lag. The Figure may be interpreted such that a disturbance in the PC at the level of interest propagates through the atmospheric column. At some lag-time, the initial disturbance has no influence on the atmospheric state, and correlations become trivial. This analysis is not inconsistent with the fluctuation dissipation theory described by Leith (1975) and applied by North et al. (1993). To provide a complementary view of the troposphere-stratosphere coupling, the Figure includes also the lag correlation based on the 50 hPa PC1 to assess the downward influence variations in the stratospheric vortex exert on the troposphere. To gauge the sensitivity of this coupling, an anomaly model experiment is performed: all Arctic sea ice is replaced by open water at 271.4K in the surface specification. A substantial additional heat source is thereby introduced at the surface via longwave radiative heating and sensible heat flux. With no sea ice, warmer lower tropospheric temperatures at the pole reduce the synoptic wave activity, and subsequently the wave forcing of the stratosphere (Noone et al., 2003).

In the control simulation the vertical coupling is substantial in the troposphere and stratosphere, although the two are largely decoupled in the mean. Large interannual variation indicates that in some years the vertical coupling is stronger while in other years there is no coherent association between the variations the stratosphere and the troposphere. This result is consistent with observational data sets and other correlative studies (e. g., Zhou et al., 2002). In the stratosphere there is evidence for a long time scale (50 days) downward modulation of disturbances in the control simulation, which is mostly absent in the no-ice experiment result. The vertical coupling across the tropopause is increased in the absence of sea ice, and reflects increased zonal symmetry in the tropospheric variations. In the control simulation, the correlations suggest tropospheric variations precede stratospheric variations by around 15 days. The signal of a tropospheric-precursor is more clearly evident in the no-ice experiment. Conversely, evidence for downward propagation of stratospheric signals over 15 days in the control is absent in the experiment. Instead there is greater persistence of stratospheric variations without sea ice. This is symptomatic of a less well formed

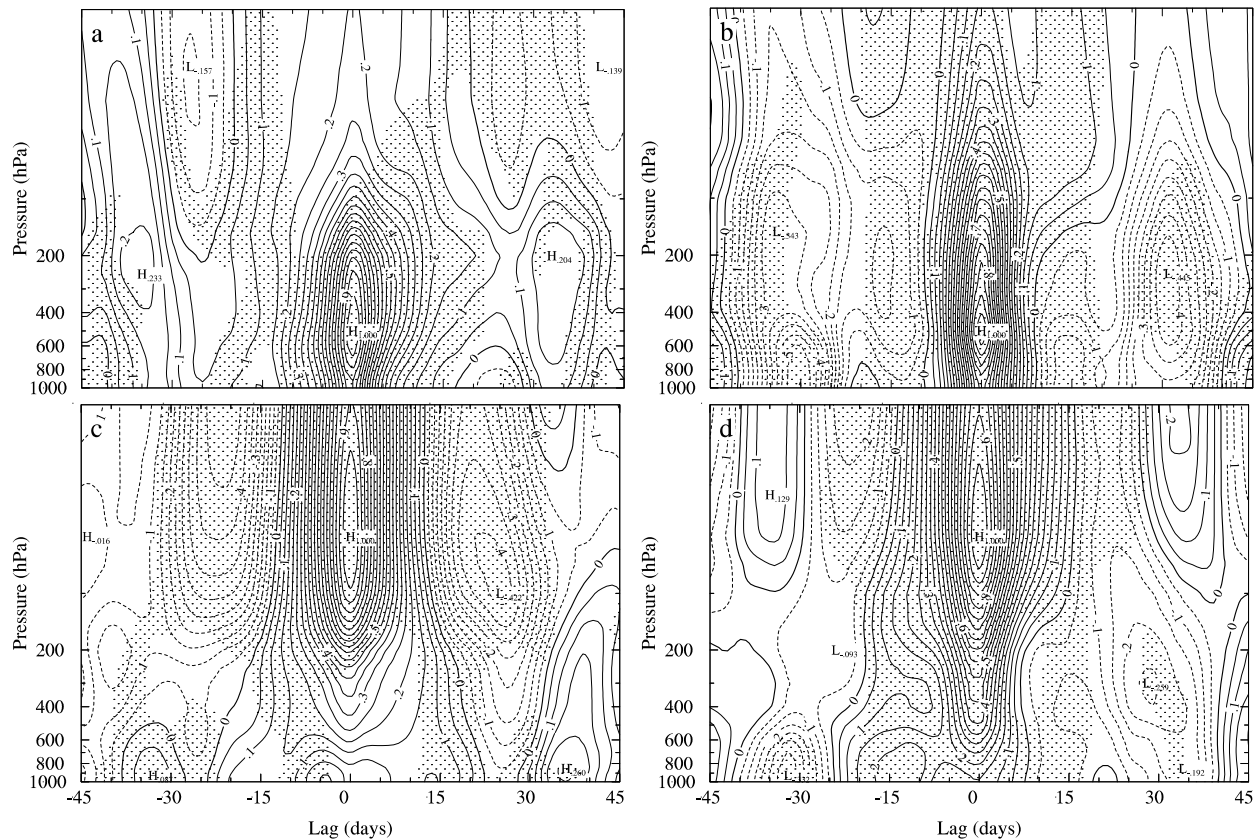


**Figure 1: Lag correlation between PC1 at (a and b) 500 hPa and (c and d) 50 hPa and PC1 computed at other levels for (a and d) control and (b and c) no sea ice experiment. Contour interval is 0.05. Stippling indicates where the interannual variation in the correlation coefficient is less than 0.3**

vortex and of a system that has less dependence on strong wave-mean interactions, as is associated with “preconditioned” stratospheric flow (Smith, 1992). Indeed this result suggests that with no sea ice, the winter circulation contrasts less distinctively with summer circulation. Specifically, the magnitude of the dynamic feedback between the location and strength of the tropospheric jet, and the generation of eddies and wave pumping that modulates the annular variations (as emphasized in many recent studies of annular modes), can be influenced by the conditions of the lower atmosphere.

## References

- Leith, C. E., 1975: Climate response and fluctuation dissipation. *J. Atmos. Sci.*, **32**, 2022-2026.
- Noone, D., Y. Yung, and R. Shia, 2003: The Northern Annular Mode response to Arctic sea ice loss and the sensitivity of troposphere-stratosphere interaction. *J. Climate*, submitted.
- North, G. R., R. E. Bell, and J. W. Hardin, 1993: Fluctuation dissipation in a general-circulation model. *Clim. Dyn.*, **8**, 259-264.
- Smith, A. K., 1992: Preconditioning for stratospheric sudden warmings: Sensitivity studies with a numerical model. *J. Atmos. Sci.*, **49**, 1003-1019.
- Zhou, S. T., A. J. Miller, J. Wang, and J. K. Angell, 2002: Downward-propagating temperature anomalies in the preconditioned polar stratosphere. *J. Climate*, **15**, 781-792.

## Sea Ice Cover Sensitivity analysis in Global Climate Model

V.P. Parkhomenko

Computing Centre of the Russia Academy of Sciences

Vavilov Str. 40 Moscow 119967 Russian Federation

E-mail: [parhom@ccas.ru](mailto:parhom@ccas.ru)

Climate model includes AGCM, ocean model and sea ice evolution model. The purpose of the work is analysis of seasonal and annual evolution of sea ice, long-term variability of a model ice cover, and also its sensitivity to some physical and model characteristics.

Results of 100 years simulations of Arctic basin sea ice evolution are analyzed. The significant (about 0.5 m) interannual fluctuations of an ice cover exist. The spectral analysis of results demonstrates 5-7 years period climate and 3-10 days synoptical ice cover fluctuations. The auto correlation function with the excluded annual and seasonal components shows data dependence with 3 days time lag.

A number of numerical experiments according to influence of some physical and model parameters on results are carried out.

The ice - atmosphere sensible heat flux 10% reduction leads to growth of mean sea ice thickness within the limits of 0.05 m – 0.1 m. However in separate spatial points there is a decreasing of thickness up to 0.5 m. The maximum increase of ice thickness is observed in the end of spring and summer seasons. It is connected with the maximal difference of air - ice temperatures in the warm period.

The analysis of average ice thickness seasonal change at decreasing on 0.05 of clear sea ice albedo shows reduction of ice thickness in a range from 0.2 m up to 0.6 m, and the maximum of change is during the summer season of intensive melting. The spatial distribution of ice thickness changes (Fig. 1) shows, that on the large part of Arctic ocean there was a reduction of ice thickness down to 1 m. However, there is also area of some increase of the ice layer basically in a range up to 0.2 m. It is located in the Beaufort sea.

The 0.05 decreasing of sea ice snow albedo leads to reduction of average thickness of ice approximately on 0.2 m, and this value slightly depends on a season. The changes in separate points are not so great (Fig. 2), as in the previous case, because the surface albedo change in polar areas is essential in summer period, and at this time snow on the significant areas of an ice cover has melted and does not influence on solar radiation absorption. There is a stable area of ice cover thickness increase as in previous case. Probably, it is connected with the atmospheric circulation, clouds and precipitation changes.

In the following experiment the ocean – ice thermal interaction influence on the ice cover is estimated. It is carried out by increase of a heat flux from ocean to the bottom surface of sea ice on 2 W/sq. m in comparison with base variant. Analysis demonstrates, that there was a reduction of average ice thickness in a range from 0.2 m up to 0.35 m (Fig. 3). There are small seasonal changes of this values.

The numerical experiments results have shown, that an ice cover and its seasonal evolution rather strongly depend on varied parameters. The spatial and seasonal structure of changes has rather complex non-uniform character, there are great areas of opposite changes. It is connected with nonlinear behavior of feedback and interactions in model system including an atmosphere, sea ice and ocean.

This work is supported by RFFI.

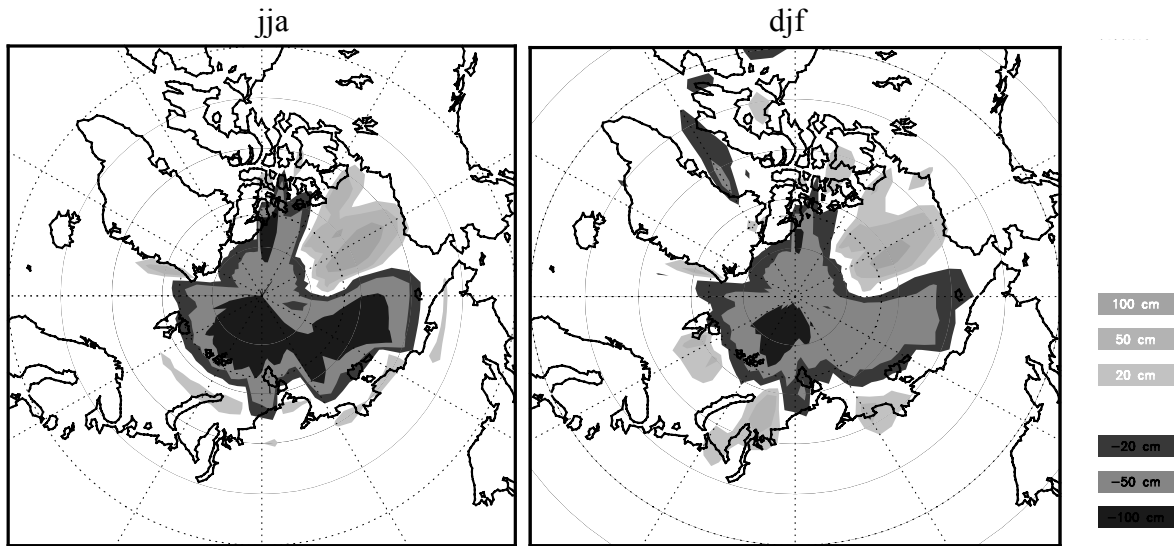


Fig. 1. Sea ice thickness changes: ice albedo decreasing experiment.

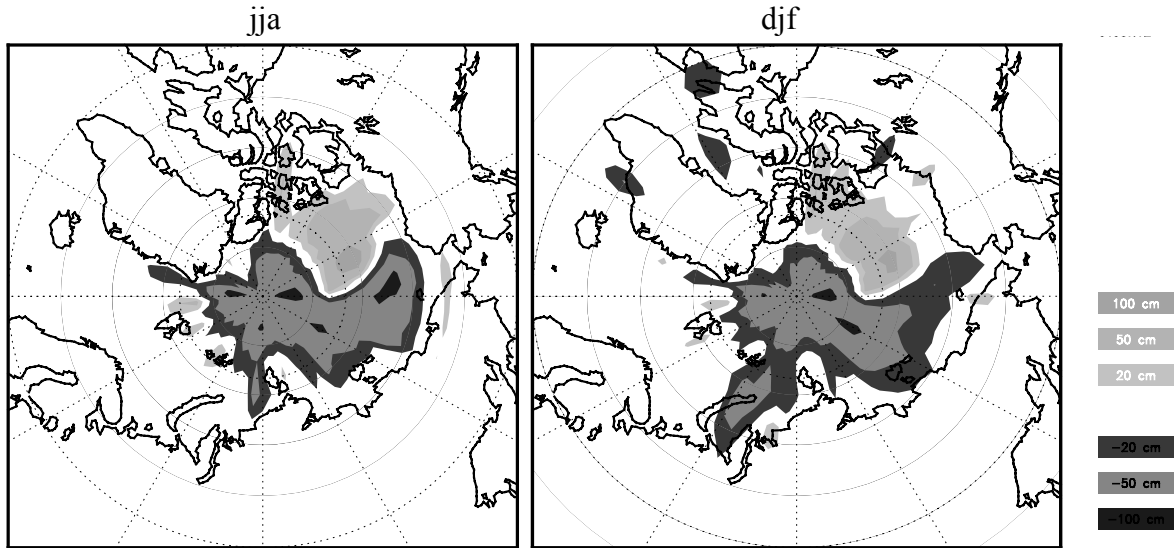


Fig. 2. Sea ice thickness changes: snow albedo decreasing experiment.

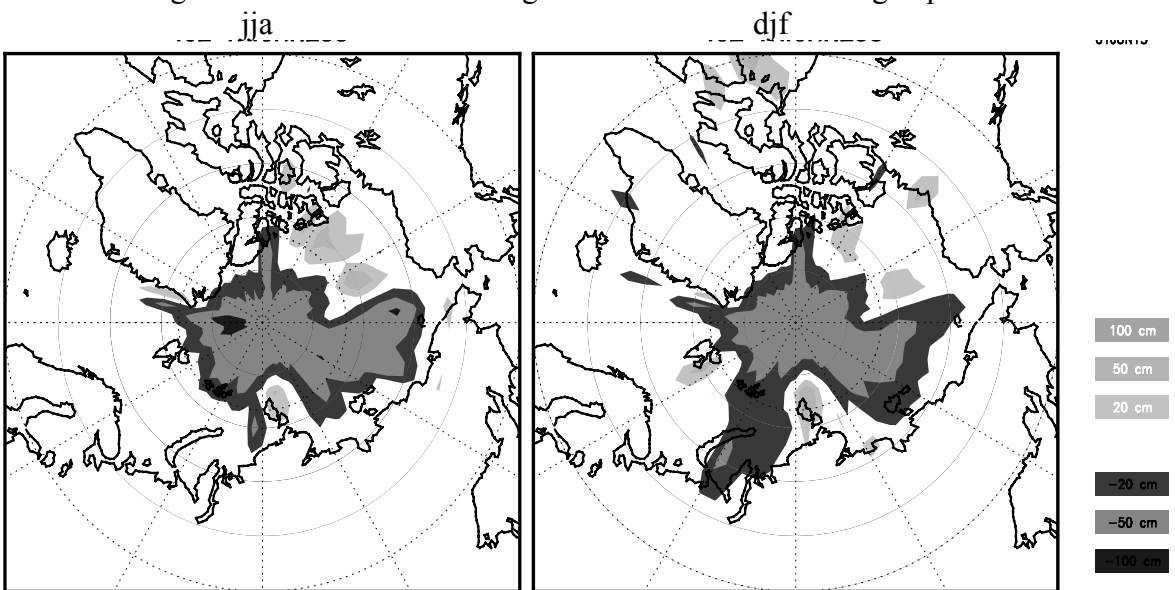


Fig. 3. Sea ice thickness changes: ocean - ice heat flux increasing experiment.

# Atmosphere-Sea Ice interaction during the Dalton Minimum within a historical simulation with ECHO-G

Sebastian Wagner

Institute for Coastal Research, GKSS-Research Centre, Germany\*

March 10, 2003

## Introduction

This paper focuses on the interdependence between sea level pressure (SLP) and the sea ice coverage (SIC) within the North Atlantic region within a historical simulation with external varying solar and volcanic forcing with the climate model ECHO-G. An explanation for the SIC-SLP interdependence will be suggested in terms of a coupled SIC-SLP mode as well as possible underlying physical mechanisms.

## SLP - SIC interdependence

In order to demonstrate the SLP-SIC interdependence, the winter months from December to March are analysed for the solar anomalous period of the Dalton Minimum (1790-1830). A reference period is chosen within the preindustrial era from 1625 to 1655. Fig.1 gives the differences between the Dalton Minimum and the reference period for the SIC (left hand side) and the SLP (right hand side).

Within the December-situation only small differences appear within the SIC and the SLP as well. The most striking feature is a SIC-dipole with an increased SIC southeast of Greenland and with an decreased SIC southwest of Greenland during the Dalton period which can also be seen within the SLP-pattern. The SIC-pattern persists throughout the whole Winter season but propagates southward on the western side. The January-situation shows a very prominent decrease within the SLP during the Dalton period over the North Atlantic and Europe but increased SLP over Northeast America. Furthermore, the SLP shows an longitudinal elongated decreased pressure zone into the Labrador sea and with slightly increased pressure over the southeastern coast of Greenland during the Dalton period. The February and March situation are quite similar. Within these two months the SIC is most pronounced within the annular cycle. The strongly reduced SIC over the Labrador sea is accompanied by low pressure anomalies, whereas the increase of SIC over the southeastern coast of Greenland and in the Nordic seas is accompanied by high pressure anomalies during the Dalton Minimum.

## Discussion

It is important to note that the Atmosphere-Sea Ice interaction is a coupled mode, where a distinction between lead and lag modes of SIC and SLP, respectively, is hard to find out. For example, a pronounced negative phase of the NAO, possibly induced via the external forcing, could initiate a SIC-pattern similar to that within the DEC-MAR SIC figures. As the SIC has a much stronger autocorrelation than the SLP-field, there is indication that the SIC-patterns tend to stimulate the SLP-fields and hence e.g. the mode of the NAO. Fig. 1 demonstrates at least that those regions influenced by changes within the SIC also show significant changes within the SLP. Furthermore the influence of the SIC-pattern on the SLP-pattern seems mostly pronounced during those month with greatest SIC.

A physical explanation for the negative and positive pressure and SIC, respectively, are possibly due to an altered atmosphere ocean heatflux exchange regime. Within regions of increased SIC the ocean can not supply the atmosphere with humidity and latent and sensible energy. The cold air over the ice covered regions sinks down increasing the SLP. Within regions of decreased SIC, the situation is reversed and the ocean induces negative pressure anomalies through slight convective processes.

## Acknowledgements

The whole 500-year simulation was carried out at the German Climate Computing Centre (DKRZ) by F. Gonzalez (GKSS) and U.Schlese (DKRZ). The forcing data for the integration were kindly supplied by T. Crowley (Texas University).

---

\*Corresponding author address: GKSS-Forschungszentrum, Max-Planck-Str.1, 21502 Geesthacht, Germany; e-mail: swagner@gkss.de

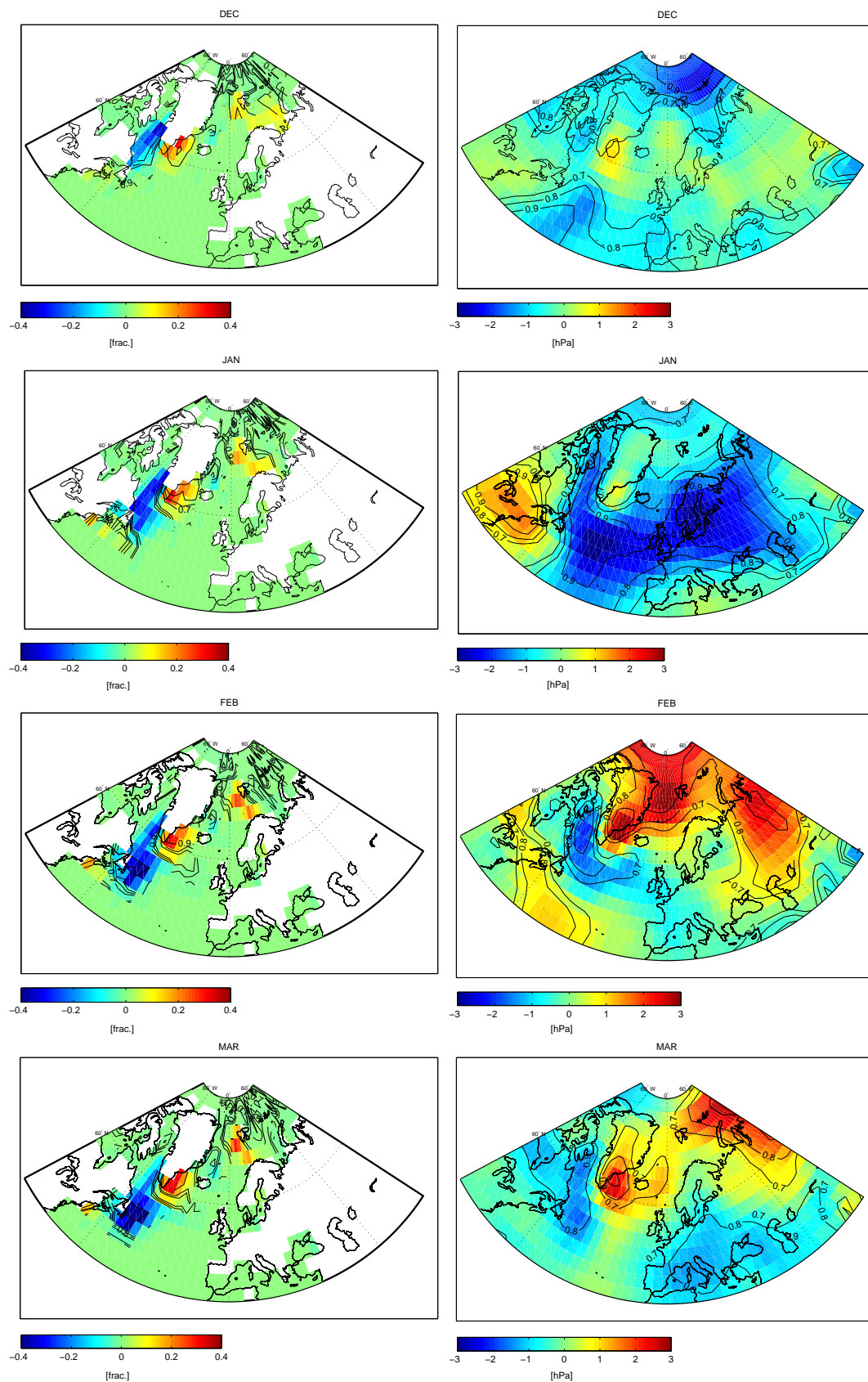


Figure 1: Differences within Sea Ice coverage (left hand side) and SLP (right hand side) between the Dalton Minimum (1790-1830) and a normal period (1625-1655) for December to March. Note the strong resemblance of SLP-anomalies within the Ice coverage anomalies around the coast of Greenland, especially in February and March. Contours denoting levels of significance  $\geq 0.7$  in steps of 0.1.

# Late Quaternary Southern Hemisphere extratropical cyclone characteristics

Richard Wardle and Ian Simmonds

School of Earth Sciences  
The University of Melbourne  
Victoria, Australia, 3010  
Email: rwardle@unimelb.edu.au

In our work we apply a modelling approach to understanding global climate and regional changes for the Australian continent that have occurred during the Last Glacial Cycle. Many previous modelling studies of palaeoenvironments have focused on the changes to the mean fields. However a more complete understanding of climate variability can be attained by an appreciation of the characteristics of that variability. Here we focus on the extratropical cyclones that are associated with weather systems over the globe. This is particularly true in the Southern Hemisphere, and especially for Australia.

The global numerical simulations are performed with an atmospheric GCM (MUGCM, see Wardle and Simmonds 2003) which successfully replicates the present day (PD) mean climatology and its variability. To elucidate the development and intensification of extratropical cyclones during a particular epoch, we apply a state-of-the-art vortex tracking scheme (Simmonds *et al.* 1999). We present here, results for the mid-Holocene (MH), some 6000 years before present. This is an epoch for which relatively large amounts of palaeo data exist (e.g., Kershaw *et al.* 2000) and for which there is a clear understanding of the climate forcings. Model boundary conditions are the same as for the PD except for the orbital forcings and the atmospheric CO<sub>2</sub> concentrations which are set appropriately.

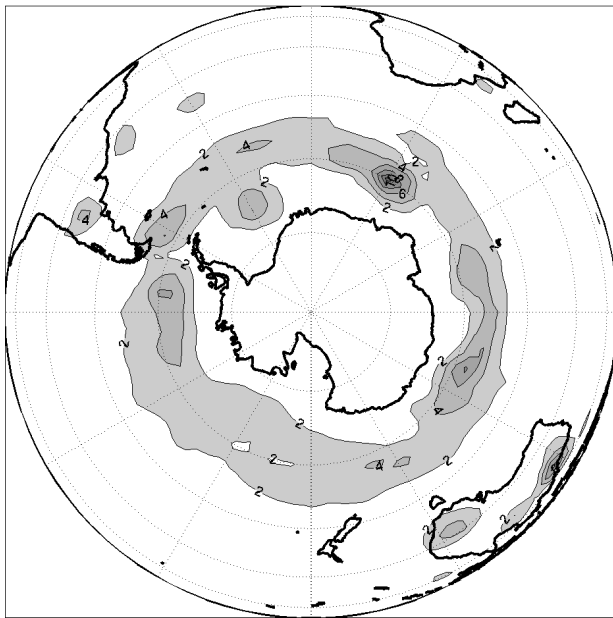
The modelled density of cyclonic systems [the mean number per analysis found in 10<sup>3</sup> (deg lat)<sup>2</sup> area] during DJF and JJA are presented in Fig. 1a-b. The seasonal anomalies in system density from those of the present day (PD) are shown in Fig. 1c-d. During DJF the differing baroclinicity of the palaeo climate yields in general more systems near 60°S except in the Pacific where the maxima lies somewhat further equatorward. For Australia there is a reduction in the number of systems over the continent consistent with the weakening of the Australian heat low during the southern summer (Wardle and Simmonds 2002). During JJA, the statistically significant changes in the number of systems are for the most part increases, particularly around 50°S, south of Australia and in the eastern Atlantic Ocean.

Kershaw A.P., P.G. Quilty, B. David, S. Van Huet, and A McMinn, 2000: Palaeobiogeography of the Quaternary of Australia. *Memoir of the Association of Australian Palaeontologists*, **23**, 471-516.

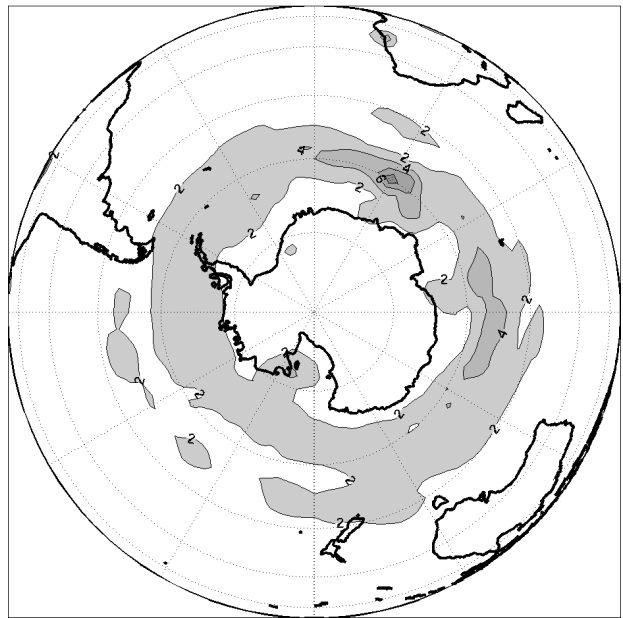
Simmonds, I., R.J., Murray, and R.M. Leighton, 1999: A refinement of cyclone tracking methods with data from FROST. *Aust. Meteor. Mag.*, Special Issue, 35-49.

Wardle, R., and I. Simmonds, 2002: Reconstructing Australian environments of the last glacial cycle through quantitative modelling. *WGNE Report No. 32. WMO/TD-No. 1105*.

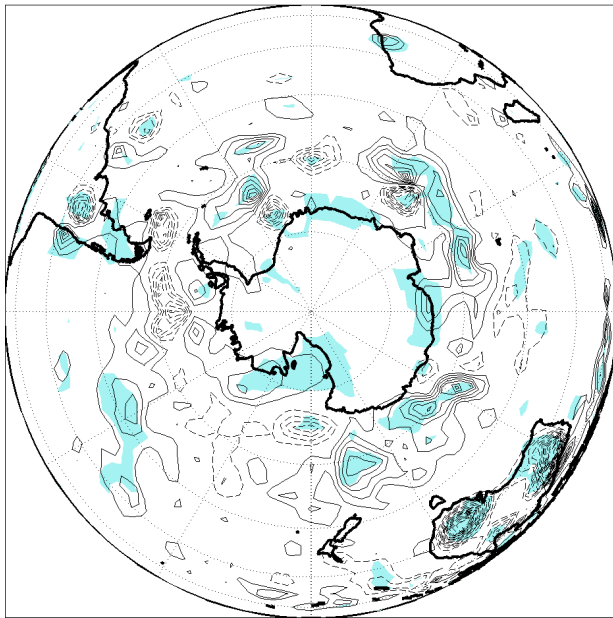
Wardle, R., and I. Simmonds, 2003: The climatology of the Melbourne University General Circulation Model version R21L9. *The University of Melbourne, School of Earth Sciences Report Number 03-01*.



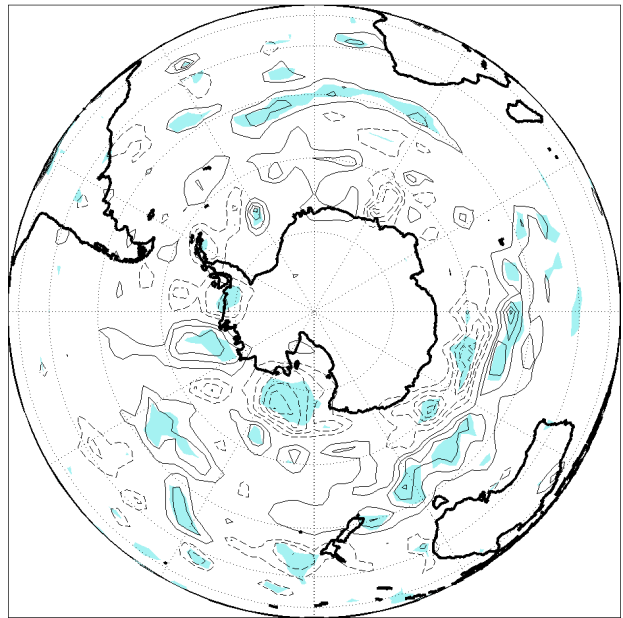
(a) MH DJF system density



(b) MH JJA system density



(c) DJF system density anomaly (PD-MH)



(d) JJA system density anomaly (PD-MH)

Figure 1: The modelled mid-Holocene (MH) cyclonic system density during (a) DJF and (b) JJA. The anomalies from present day (PD) are presented in (c) and (d) for DJF and JJA respectively. In (c) and (d), negative (positive) anomalies are dashed (solid) and anomalies significant at the 95% level are shaded. The contour intervals are (a)-(b)  $2 \times 10^{-3}$  (deg lat) $^{-2}$  and (c)-(d)  $0.2 \times 10^{-3}$  (deg lat) $^{-2}$ .